



Universidad Autónoma
de Madrid

Biblos-e Archivo
Repositorio Institucional UAM

Repositorio Institucional de la Universidad Autónoma de Madrid

<https://repositorio.uam.es>

Esta es la **versión de autor** del artículo publicado en:
This is an **author produced version** of a paper published in:

IEEE Transactions on Antennas and Propagation 69.5 (2021): 2546 - 2559

DOI: <https://doi.org/10.1109/TAP.2020.3033965>

Copyright: © 2021 IEEE

El acceso a la versión del editor puede requerir la suscripción del recurso
Access to the published version may require subscription

Triple Radiation Pattern Monopulse Horn Feed with Compact Single-layer Comparator Network

Lucas Polo-López, Juan Córcoles, Jorge A. Ruiz-Cruz, José R. Montejo-Garai and Jesús M. Rebollar

Abstract—A monopulse horn feed with a triple radiation pattern (sum, elevation difference and azimuthal difference) operating at 35 GHz is presented. The device consists of three main parts: a spline profiled horn, a mode converter that generates the modal field combinations that produce each radiation pattern, and a very compact single-layer monopulse comparator network. Unlike other state-of-the-art designs, the novel feed is based on a triple radiation pattern horn with a mode converter excited by a comparator network implemented in a single level for improving the compactness and easing a quasi 2D manufacturing. The kernel of this network is a novel 180° H-plane waveguide coupler with in-line ports, which avoids any additional phase compensation in the routing waveguide sections used in other works. The design process of the Ka-band antenna feed is described, and simulated results for the three radiation patterns and their associated reflection coefficients are presented. The prototyping process is outlined and the obtained experimental results are compared with the simulated ones showing very good agreement and validating the design process.

Index Terms—Radar antennas, horn antennas, antenna feeds, radar tracking, millimeter wave radar, directional couplers.

I. INTRODUCTION

SINCE it was initially conceived [1], radar technology has experienced an enormous development and nowadays it constitutes the keystone of a wide range of different applications. These are found not only in the military area [2], [3], but also in other civil scenarios like air traffic control [4], [5], remote sensing [6], [7], the automotive sector [8], [9], meteorology [10], [11] or space debris detection among others [12], [13]. In Ka-band, as the design in this paper, different radar applications are found, like airport surveillance or traffic enforcement cameras activated by radar [14]–[16].

Monopulse tracking systems can obtain the angle-error information from just a single received pulse by using, simultaneously, more than one antenna beam [17, Ch. 5] [18, Ch. 1]. These systems have undergone a great evolution. Originally, monopulse feeds were implemented using four [19], [20] (or in certain cases even more [21]) squared horns. A monopulse comparator network is in charge of properly combining the signals of the four horns to produce the sum and difference radiation patterns. The main disadvantage of this approach is that the configuration that achieves an optimal illumination of the reflector by the sum pattern is not the best one for the difference patterns [22]. To solve this, one possible option is to use a multimode horn or a waveguide feed [23, Ch. 8].

There are two main approaches to the design of multimode monopulse feeds. In the first approach the higher order modes are obtained by abruptly joining two or more rectangular waveguides into a greater waveguide section [24]–[27]. The sum and difference patterns are

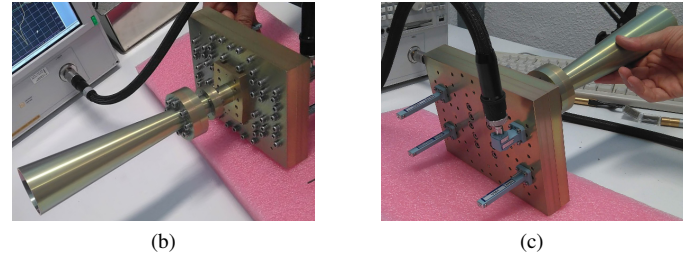
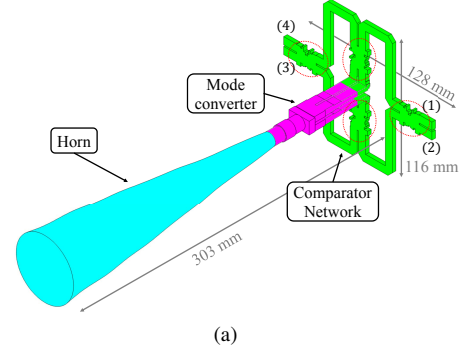


Fig. 1. (a) 3D representation of the inner parts of the monopulse Ka-band antenna feed. The input ports are numbered 1 for sum, 2 for elevation difference, 4 for azimuthal difference and 3 is not used. The 180° hybrid couplers are circled in red. (b) and (c) are photographs of the manufactured prototype.

obtained by combining the signals of the rectangular waveguides using a comparator network, as in the case of the monopulse feeds with several horns. The second approach consists in generating the higher order modes using a beam-forming network with different mode extractors placed along a multimode open ended waveguide [28]–[30]. The design presented in this work belongs to the first type, which leads to more compact and lower cost feeds, suitable for systems produced in large numbers [23, Ch. 8].

The proposed monopulse horn feed at Ka-band (shown in Fig. 1) presents distinctive characteristics regarding the feed architecture and its components, over other configurations in the state of the art [25], [31]–[38]. First, the feed produces a triple radiation pattern (sum, azimuthal difference and elevation difference patterns), while other works present just a sum and a single difference pattern [31]–[34], leading to relevant differences in the feeder architecture. In our work, this triple radiation pattern is achieved with a spline profile high-gain horn, connected by a mode converter to a very compact comparator network. This mode converter acts as a multi-mode transformer between the rectangular interfaces of the comparator network waveguides and the circular section of the horn. Thanks to the use of a circular section horn, it is possible to obtain a sum radiation pattern with rotational symmetry [25]. Second, the comparator network has been implemented in a single-level, perpendicular to the axis of the horn. This configuration maximizes the feed compactness and reduces drastically the manufacturing complexity of the comparator [36]–[38]. Third, novel 180° waveguide hybrid couplers have been introduced

Manuscript received Month XX, 2020.

This work was supported by Spanish Government (Agencia Estatal de Investigación, Fondo Europeo de Desarrollo Regional) under grants TEC2016-76070-C3-1/2-R (AEI/FEDER, UE) and S2013/ICE-3000 (Comunidad de Madrid).

L. Polo-López, J. Córcoles and J. A. Ruiz-Cruz are with the Escuela Politécnica Superior, Universidad Autónoma de Madrid, Madrid, Spain (e-mail: lucas.polo@uam.es).

J. R. Montejo-Garai and J. M. Rebollar are with Information Processing and Telecommunications Center, Universidad Politécnica de Madrid, Madrid, Spain.

TABLE I
SPECIFICATIONS FOR THE DIFFERENT RADIATION PATTERNS.
THE SPECIFICATIONS FOR BOTH DIFFERENCE PATTERNS ARE THE SAME.

Feature	Sum	Difference
Waveguide ports	WR-28	WR-28
Band of operation (GHz)	34.6-35.4	34.6-35.4
Return loss (dB)	> 20	> 20
Isolation between ports (dB)	> 30	> 30
Gain (dBi)	24.0-24.5	21.5-22.0
Beamwidth at -14 dB ($^\circ$)	12 ± 2	12 ± 2
Polarization	Linear	Linear
Crosspolarization (dB)	< -25	< -20
SLL w.r.t. Sum max (dB)	< -25	< -15



Fig. 2. Schematic representation of a single aperture multimode monopulse waveguide feed: (a) Lateral view. (b) Front view.

for being able to synthesize the full comparator using only H-plane components in a single level. The novel couplers avoid the need of additional phase shifters [35] or waveguide sections distributed in different levels for compensating the phase differences [25] required by other comparator networks.

II. OPERATING PRINCIPLE

The proposed monopulse horn feed is represented in Fig. 1 (a). The complete feed can be conceptually divided in three components: horn antenna, mode converter and comparator network. This feed generates one sum radiation pattern and two difference patterns (elevation and azimuth) when excited by ports 1, 2 and 4, respectively. Port 4 is not used and it is terminated with a matched load. The specifications for each of the radiation patterns are presented in Table I.

The designed multimode feed consists of a circular waveguide (with a diameter large enough to allow multimode propagation in the operation band) that is excited by four rectangular waveguides operating in the monomode regime (i.e. monomode excitation by the TE_{10} mode). A schematic representation of this kind of feed can be found in Fig. 2. The feed has to be designed in such a way that it produces the different radiation patterns depending on the combination of excitations at the four waveguide ports.

The sets of excitations at the input of the mode converter that lead to the different radiation patterns are represented in Fig. 3. When all the ports are excited in phase, the sum pattern is produced. When the upper and lower ports are excited with a 180° phase shift, then the elevation difference pattern is produced. Finally, when the 180° phase shift occurs between the left and right ports, the azimuthal difference pattern is obtained. Fig. 3 also shows that each excitation exhibits a different electrical symmetry along the vertical and horizontal symmetry planes of the feed.

A spline profile horn has been chosen instead of a corrugated profile horn, since the spline profile is easier to manufacture [39]. Each radiation pattern will be produced by the combination of two circular waveguide modes with the appropriate complex amplitudes at the horn aperture, as it will be shown later in subsection III-B.

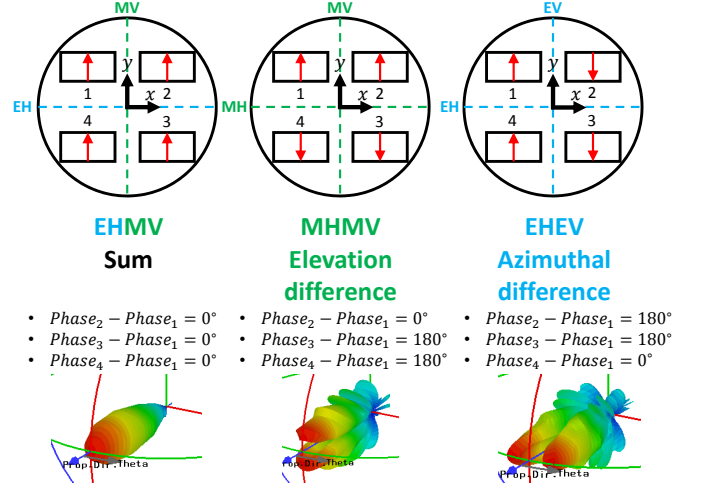


Fig. 3. Excitations at the rectangular ports of a multimode monopulse feed that produce the different radiation patterns, and 3D representation of each pattern. EHMV stands for “Electric Horizontal, Magnetic Vertical”, MHMV for “Magnetic Horizontal, Magnetic Vertical” and EHEV for “Electric Horizontal, Electric Vertical”, where H is the horizontal plane ($y = 0$) and V is the vertical plane ($x = 0$), accounting for the required conditions to be fulfilled in the symmetry planes.

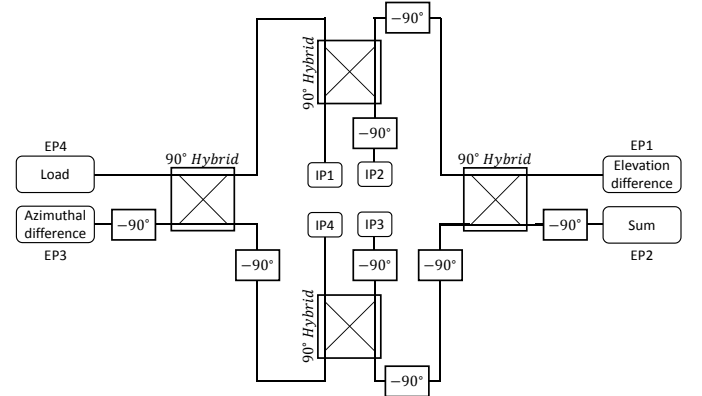


Fig. 4. Circuitual representation of the comparator network. The internal ports (IPs) are connected to the mode converter and the external ports (EPs) are connected to the transceiver system; except EP4, which is terminated with a matched load.

III. DESIGN OF THE COMPONENTS

A. Comparator network

This eight port device, shown in Fig. 4, provides the different excitations at the rectangular ports of the mode converter. A common circuitual representation of the comparator network can be found in Fig. 4, using standard components as 90° hybrids and 90° phase shifters. When an external port (EP) is excited, the signal gets divided with equal amplitude between the four internal ports (IPs). Its phase at each of these ports depends on the excited EP, and the different options correspond with the excitation patterns represented in Fig. 3. Due to the symmetry of the structure, EP4 produces an excitation at the IPs that presents a MHEV field pattern symmetry. This excitation of the mode converter has no use for the monopulse system and, therefore, this EP4 is unused and terminated with a matched load to avoid any undesired reflections.

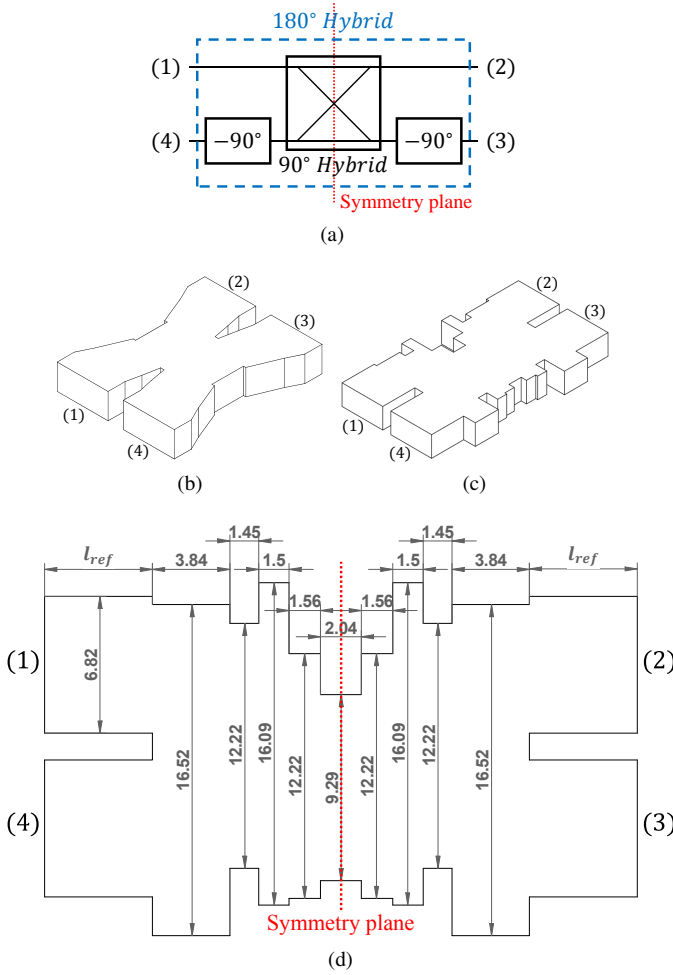


Fig. 5. (a) Circuit scheme of the 180° hybrid coupler implemented for the comparator network. (b) 3D representation of a classic H-plane 90° hybrid short slot coupler. (c) 3D and (d) top view of the 180° hybrid coupler H-plane waveguide implementation (dimensions in mm) in Ka-band, where the phase shifters have been absorbed in the middle section of the coupler.

The scattering matrix of a 90° hybrid coupler is:

$$S = \frac{-1}{\sqrt{2}} \begin{bmatrix} 0 & j & 1 & 0 \\ j & 0 & 0 & 1 \\ 1 & 0 & 0 & j \\ 0 & 1 & j & 0 \end{bmatrix}. \quad (1)$$

As it can be appreciated in Fig. 4, each coupler presents two adjacent 90° phase shifters. The combination of these two elements (as depicted in Fig. 5 (a)) can be seen as a 180° hybrid with the following scattering matrix:

$$S = \frac{-j}{\sqrt{2}} \begin{bmatrix} 0 & 1 & -1 & 0 \\ 1 & 0 & 0 & -1 \\ -1 & 0 & 0 & -1 \\ 0 & -1 & -1 & 0 \end{bmatrix}. \quad (2)$$

One well-known waveguide device that implements a 180° hybrid is the magic-T [40, Ch. 7]. However, the use of three-dimensional elements like the magic-T prevents the implementation of the comparator network in a single level [36]–[38], increasing therefore the manufacturing complexity. Moreover, the S-matrix provided by a magic-T or a rat race structure is not row equivalent to (2) (i.e., (2) cannot be achieved with these networks without using further components). An alternative solution consists in implementing the

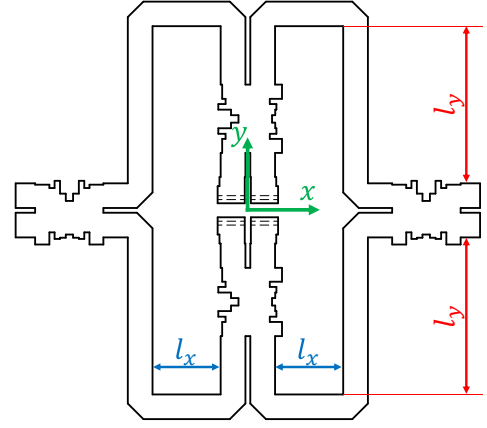


Fig. 6. Top view of the Ka-band waveguide implementation of the monopulse comparator network. Lengths l_x and l_y can be chosen arbitrarily since they do not have any electrical restriction.

comparator network using 90° hybrid couplers and quarter wavelength waveguide sections to obtain the phase shifts, like it is done in [25]. Nevertheless, this solution does not either allow to implement the comparator network in a single level, since it is necessary to fold the quarter wavelength lines in order to adjust the different physical lengths of each path. In addition, the use of quarter wavelength waveguide sections as 90° phase shifters limits the maximum achievable bandwidth. This bandwidth limitation issue also appears in [41], where quarter wavelength sections are also used as 90° phase shifters. Other alternatives like the design of more sophisticated phase-shifting structures can overcome the bandwidth issue associated to quarter wavelength waveguide sections but they still conflict with achieving a compact network due to the relatively big size of these phase-shifting elements [35].

On the other hand, the solution proposed in this work enables the implementation of the comparator network in a single level. This allows to reduce the complexity of the device manufacturing, since it can be built in just two parts: a body where the waveguides are machined and a cover or lid. However, this single level topology is not something trivial to achieve, as it is shown by several state-of-the-art designs where multilevel networks are employed [25], [36]–[38]. In this work a very compact single level solution is achieved, as shown in Fig. 6, thanks to the introduced 180° couplers. In the case that an even more compact design would be pursued, the comparator network could be implemented in substrate integrated waveguide (SIW) to reduce the waveguide height at the expense of increased power losses.

The device, which presents an H-plane configuration, is depicted in Fig. 5 (c). It is based on the Riblet short-slot hybrid [42] (see Fig. 5 (b)), whose profile has been thoroughly modified (by introducing corrugations) to absorb the phase shifting within the intermediate coupling region. Moreover, one plane of symmetry of the original structure has been removed, leaving the central symmetry plane as in Fig. 5 (d). This is essential to drastically change its phase response in order to achieve the behaviour described by the scattering matrix in (2). With this solution it is not necessary to have waveguide sections of different lengths between the couplers to compensate for phase differences. In fact, the length of the waveguides that connect the different couplers (l_x and l_y in Fig. 6) do not have any electrical restriction, since they do not affect the relative phase differences between the different paths. They can be selected by the designer to meet only geometrical constraints related to the manufacturing.

The stepped profile of the proposed 180° coupler (which is detailed in Fig. 5 (d)) is especially suited for a mode-matching analysis and

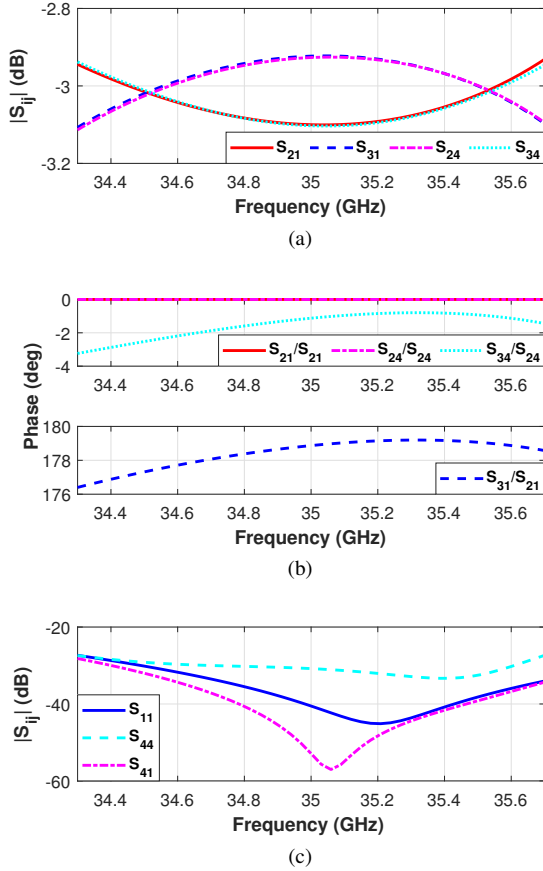


Fig. 7. Full-wave simulation of the scattering parameters corresponding to the designed 180° hybrid waveguide coupler in Fig. 5 (d): (a) Transmission to through and coupled ports. (b) Phase difference. (c) Reflection at the input and transmission to isolated port.

optimization of the structure [43], [44, Ch. 6]. Fig. 7 represents the simulated scattering parameters of the 180° coupler in Fig. 5 (d). Since the device presents a symmetry plane along its vertical axis, only the parameters corresponding to the excitation of ports 1 and 4 are plotted. The minimum width of the stubs has been constrained during the optimization process for allowing its manufacturing (further details are presented in section V). Moreover, the structure is optimized with enough margin with respect to the bandwidth limits in order to prevent degradation caused by manufacturing tolerances.

As Fig. 7 (a) shows, the signal from port 1 or 4 is divided with equal amplitude between ports 2 and 3. The relative phase shift between the two output signals depends on the input port, as it is shown in Fig. 7 (b). For the phase reference, the TE_{10} mode at the ports is polarized along y in Fig. 3. When port 1 is excited the output signals at ports 2 and 3 present a phase shift of 180°. On the other hand, when the excitation is applied to port 4, the output signals are in phase. Finally, Fig. 7 (c) shows that both the return losses when exciting either port 1 or 4 and the isolation between these two ports are better than 30 dB for the operation bandwidth in Table I.

Additionally, the implementation of the waveguide comparator network requires E- and H-plane waveguide bends. The E-plane bend, which is only used at the ports of the network, has been designed with a stepped profile to ease the manufacturing by computer numerical control milling. The H-plane bends are used at the coupler ports. As it can be seen in Fig. 8, both E- and H-plane bends are well matched and therefore they have been incorporated to the comparator network seamlessly.

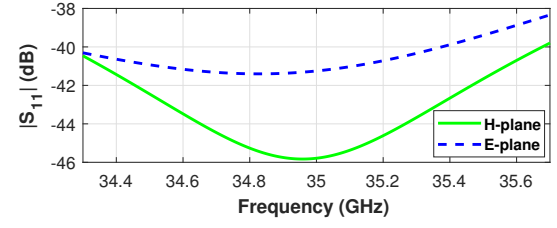


Fig. 8. Full-wave simulation of the reflection at the input of the designed 90° waveguide bends.

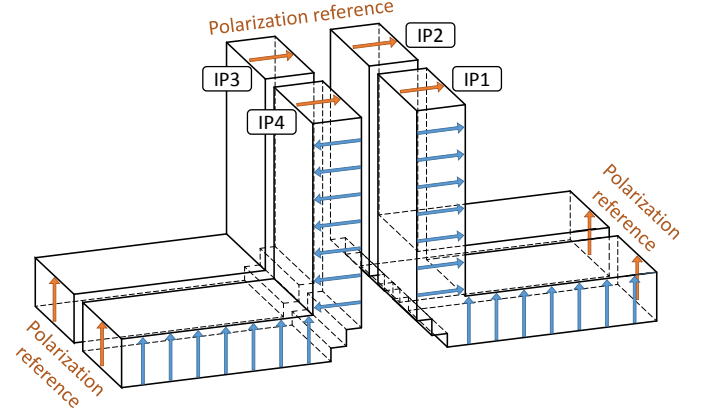


Fig. 9. The E-plane bends of the comparator network introduce a 180° phase-shift to the signals at IP3 and IP4 with respect to the circuit design of Fig. 4.

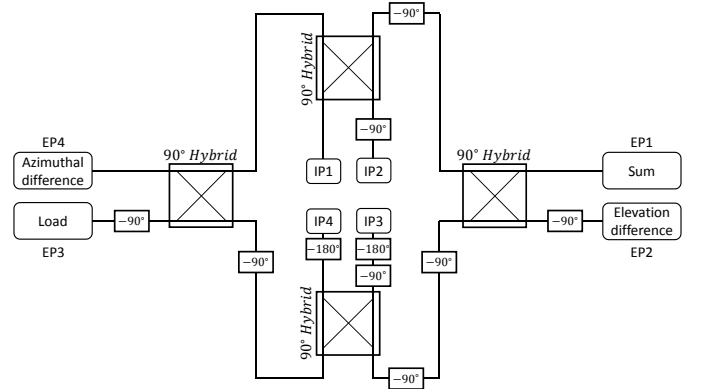


Fig. 10. Circuitual representation of the comparator network, updated to include the phase shift produced by the E-plane bends. The internal ports (IPs) are connected to the mode converter and the external ports (EPs) are connected to the transceiver system; except EP3, which is terminated with a matched load.

An important issue regarding the E-plane bends is that, since the polarization of the four IPs in the circuitual scheme of Fig. 4 is assumed to be along y (according to Fig. 3), the 90° E-plane bend introduces a 180° phase shift to the signal of ports IP3 and IP4. This is illustrated in Fig. 9. Therefore the circuitual scheme presented in Fig. 4 must be updated. The new scheme is presented in Fig. 10 and, as it can be observed, the phase shift introduced by the E-plane bends alters the correspondence between the external ports and their associated radiation patterns. The new correspondence is: EP1, sum; EP2, elevation difference; EP3, not used; EP4, azimuthal difference.

The obtained values for the reflection at each one of the EPs of the complete comparator network are represented in Fig. 11. The four ports are well matched with a return loss level better than 25 dB for

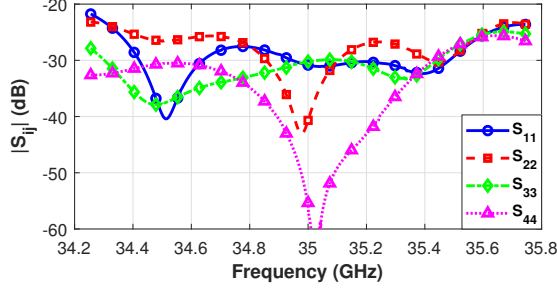


Fig. 11. Full-wave simulation of the comparator network in Fig. 1 (a). Reflection coefficient at the external ports.

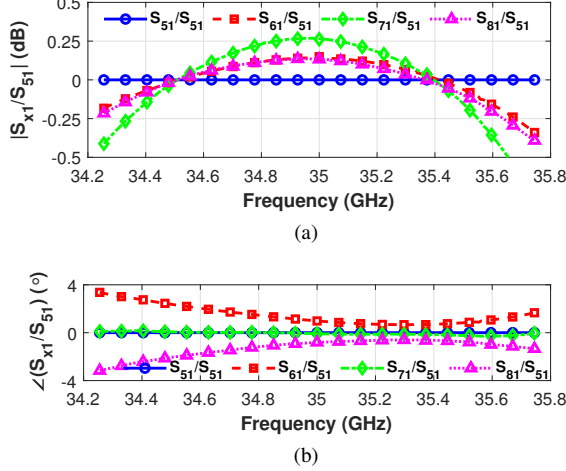


Fig. 12. Full-wave simulation of the comparator network in Fig. 1 (a). Transmission coefficients to the four IPs (numbered 5 to 8) when EP1 is excited, normalized to S_{51} : (a) Magnitude. (b) Phase.

the design band. The transmission to the four IPs from each of the EPs is depicted in Figs. 12–15 (please note that in these figures ports EP1 to EP4 are numbered 1 to 4 and ports IP1 to IP4 are numbered 5 to 8, respectively). These figures show that in all the cases the power is divided equally between the IPs and in all the cases the relative phase shift between these ports is the adequate (according to Fig. 3) to generate the required radiation patterns.

B. Horn antenna

The three desired radiation patterns are generated by a proper field distribution at the antenna aperture. Each field distribution is the combination of two circular waveguide modal fields with the amplitude and phase presented in Table II. These modal field combinations are produced by the mode converter at the horn input, and the profile of the horn is designed so that the device allows the propagation of these modes without altering their relative amplitude and phase shift while also obtaining a good return loss level. Please note that, in this work, the modal field functions of a circular waveguide are denoted by $TE_{qr}^{c/s}, TM_{qr}^{c/s}$, where q and r are, respectively, the number of angular and radial variations, while the superscript c/s accounts for the two different trigonometric functions \cos/\sin of the modal field functions in the circular waveguide.

The horn has been designed with a spline profile. Although the bandwidth performance obtained with this kind of profile is not as good as that achieved by corrugated ones, spline profile horns are much easier to manufacture [39]. This kind of profile is defined by the surface of revolution created by a spline curve rotating around the horn longitudinal axis.

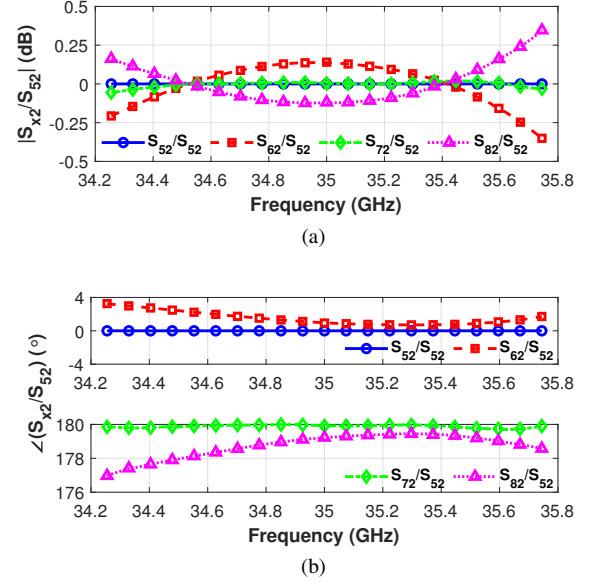


Fig. 13. Full-wave simulation of the comparator network in Fig. 1 (a). Transmission coefficients to the four IPs (numbered 5 to 8) when EP2 is excited, normalized to S_{52} : (a) Magnitude. (b) Phase.

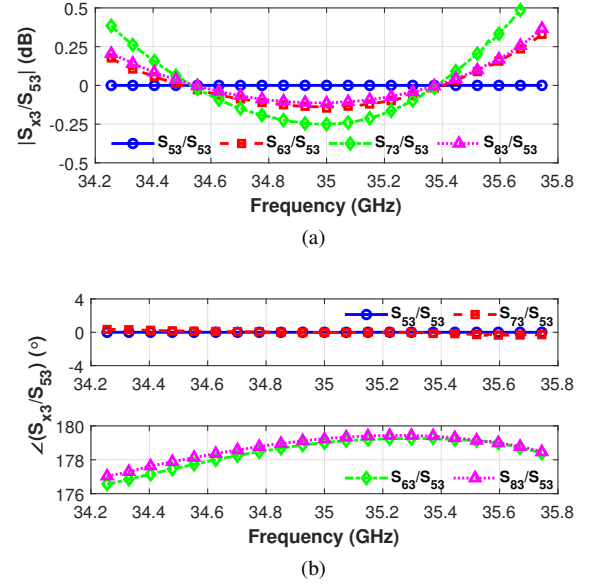


Fig. 14. Full-wave simulation of the comparator network in Fig. 1 (a). Transmission coefficients to the four IPs (numbered 5 to 8) when EP3 is excited, normalized to S_{53} : (a) Magnitude. (b) Phase.

TABLE II
COMPLEX MODAL AMPLITUDES THAT PRODUCE
THE THREE MONOPULSE RADIATION PATTERNS.

	Sum		Azim. Diff.		Elev. Diff.	
Mode	TE_{c11}	TM_{s11}	TE_{c21}	TE_{c01}	TM_{c01}	TE_{s21}
Magnitude	1.00	0.38	1.00	1.00	1.00	1.20
Phase	0°	180°	0°	180°	0°	0°

This curve is defined by a set of reference radii that the curve must pass across. By modifying these radii the behaviour of the profile can be adjusted. Initially (see Fig. 16 (a) for an example with six sections) the reference points are equispaced along the horn length (l_1 to l_6 have the same length) and their corresponding radii values

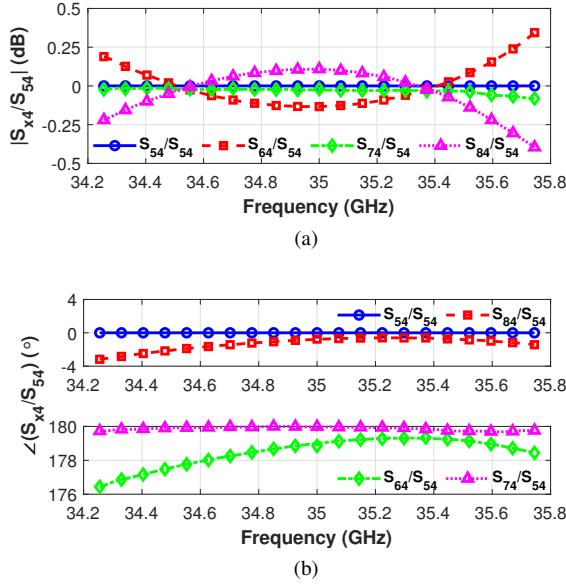


Fig. 15. Full-wave simulation of the comparator network in Fig. 1 (a). Transmission coefficients to the four IPs (numbered 5 to 8) when EP4 is excited, normalized to S_{54} : (a) Magnitude. (b) Phase.

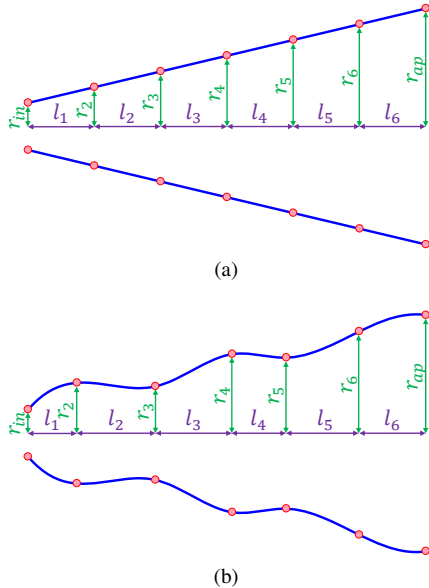


Fig. 16. (a) Conical profile horn. (b) Spline profile horn.

(r_{in} to r_{ap}) are also equispaced between the input and aperture radii. Applying the spline curve to this set of reference radii yields a conical profile. To obtain the horn profile that achieves the desired behaviour, a cost function has been defined and the set of reference radii, as well as their spacing, have been optimized in order to minimize this cost function. An example of a spline profile is shown in Fig. 16 (b), although in this case the values of the reference radii have been exaggerated in order to magnify the curvature of the profile for illustrative purposes.

During the optimization process, the characterization of the horn has been carried out using a mode-matching approach [45] which consists in using the mode-matching method [43], [44, Ch. 6] to analyse the horn profile and determine the modal field distribution at the aperture. Then the radiation pattern produced by the horn can be obtained by applying the equivalence principle of radiating apertures

[46, Ch. 7] to this aperture field distribution. It should be stressed that, due to the high number of iterations required by the optimization process, it would have been impractical to compute the response of the horn using an analysis tool based on a general numeric method.

In order to speed up the mode-matching analysis, instead of carrying out one single simulation where all the possible modes of the structure are considered, three different simulations have been performed. In each simulation, only the set of circular waveguide modes generated by the three different excitations of Fig. 3 has been taken into account. This allows to reduce the number of modes considered in each simulation, since each radiation pattern imposes different boundary conditions in the principal xz and yz planes of the horn (please see Fig. 3). This significantly reduces the computation time due to the smaller size of the matrices appearing in the mode-matching analysis. For a certain symmetry (i.e. one of the three radiation patterns) the cost function is:

$$C = \sum_{n=2}^{N_{ap}} |S_{2(n),1(1)}| + |S_{2(1),1(2)}| + \sum_{n=3}^{N_{ap}} |S_{2(n),1(2)}| + \left| \angle \frac{S_{2(2),1(2)}}{S_{2(1),1(1)}} \right|, \quad (3)$$

where $S_{w(x),y(z)}$ represents the scattering parameter associated to the x -th mode of the w -th port when the z -th mode of the y -th port is excited. Port number 1 represents the horn input and port number 2 the horn free space aperture. The phase term in (3) is computed in radians. N_{ap} corresponds to the number of modes considered at the horn aperture during the mode-matching analysis. This number is adjusted to different values at different stages of the design process depending on the desired level of accuracy. During the initial stages of the design process it is adjusted to 80 modes in order to accelerate the simulation of the horn. Then, when an initial set of design parameters has been obtained, N_{ap} is increased progressively (and the design parameters are adjusted after each increment of N_{ap}) until convergence of the mode-matching results is guaranteed. For the presented device this occurs for $N_{ap} = 200$. Since the horn must produce three distinct radiation patterns, the total cost function can be computed as:

$$C_H = C]_{EHMV} + C]_{EHEV} + C]_{MHMV}. \quad (4)$$

Twelve reference radii values have been used to define the profile of the horn. Two of these points correspond to the input ($r_{in} = r_1$) and aperture ($r_{ap} = r_{12}$) radii, and therefore they are not modified during the optimization process. The horn input radius is fixed to $r_{in} = 5.64$ mm, which allows the propagation of the six modes required to generate the three radiation patterns while any higher order mode is at cut-off. The aperture radius has been chosen to achieve a directivity level of 24.5 dBi for the sum radiation pattern, which yielded $r_{ap} = 3.2\lambda_0 = 27.43$ mm. Choosing the length of the horn (l_H) poses a trade-off between the compactness of the antenna and the achieved return loss level. Several designs have been carried out, progressively diminishing this parameter until an optimal value of $l_H = 214.86$ mm was found.

During the optimization process it was established that $r_i > r_{i-1}$ to prevent the algorithm from converging to a solution with inner cavities that would have been more difficult to manufacture. The obtained reference radii are presented in Table III.

C. Mode converter

The (multi-)mode converter is the component in charge of, starting from the excitations defined in Fig. 3, generating the circular waveguide modal field combinations of Table II at the horn input.

TABLE III
VALUES (IN mm) OF THE REFERENCE RADII AND THEIR SPACING
FOR THE DESIGNED SPLINE PROFILE HORN.

i	1 (i_n)	2	3	4	5	6	7	8	9	10	11	12 (a_p)
r_i	5.64	7.71	8.62	11.33	13.97	15.68	18.05	20.33	22.16	23.98	25.73	27.43
l_i	19.34	19.93	22.56	16.01	18.05	16.30	18.99	20.65	18.29	20.52	24.25	—

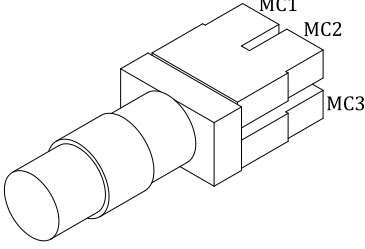


Fig. 17. 3D representation of the mode converter inner parts. The rectangular ports are numbered MC1 to MC4 (note that in the figure MC4 is hidden).

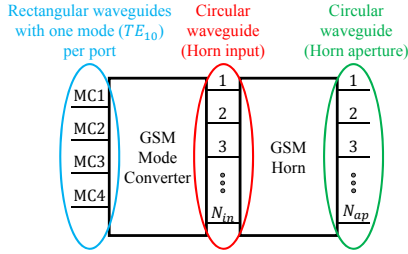


Fig. 18. Schematic representation of the cascading between the mode converter and horn Generalized Scattering Matrices (GSM).

To achieve this, the device presents four rectangular waveguide ports (MC1 to MC4) that are connected to the corresponding IPs of the comparator network. As Fig. 17 shows, first these ports are joined in pairs by two wide independent waveguide sections, which are later merged. After that, the rectangular waveguide is transformed to a circular waveguide whose radius allows the propagation of the six modes in Table II. Thanks to two circular waveguide steps the complex amplitudes of these modes are adjusted [23, Ch. 8] in order to produce the desired field distributions at the horn input.

This device has also been optimized using a mode-matching tool to compute its response and, like in the case of the horn antenna, the symmetries of the structure and the excitations have been exploited to reduce the computation time. The cost function of the mode converter has been defined in terms of the reflected wave at each rectangular port and the complex amplitude of each of the modes at the circular port. Nevertheless, to obtain a more accurate modelling of the problem, at each iteration of the optimization process the Generalized Scattering Matrix (GSM) of the mode converter has been cascaded with the (already computed and stored) GSM of the horn. Then, the complex modal amplitudes taken into account at the cost function are those at the horn aperture. This cascading process is illustrated in Fig. 18, where ports 1 to N_{ap} correspond to the modes considered at the horn aperture for the mode-matching analysis. It is important to note that the GSM of the horn is computed just once before starting the optimization process and, therefore, its cascading with the GSM of the mode converter can be done efficiently.

The cost function used for the mode converter optimization is defined as:

$$C_{MC} = C_1 + 3 \cdot C_2 + C_3 + C_4, \quad (5)$$

$$C_1 = \left| \frac{S_{2(2),1(1)}^{EHMV}}{S_{2(1),1(1)}^{EHMV}} - 0.38 \right| + \left| \frac{S_{2(2),1(1)}^{EHMV}}{S_{2(1),1(1)}^{EHMV}} - 1 \right| + \left| \frac{S_{2(2),1(1)}^{MHMV}}{S_{2(1),1(1)}^{MHMV}} - 1 \right|, \quad (6)$$

$$C_2 = \left| \angle \frac{S_{2(2),1(1)}^{EHMV}}{S_{2(1),1(1)}^{EHMV}} - \pi \right| + \left| \angle \frac{S_{2(2),1(1)}^{EHMV}}{S_{2(1),1(1)}^{EHMV}} - \pi \right| + \left| \angle \frac{S_{2(2),1(1)}^{MHMV}}{S_{2(1),1(1)}^{MHMV}} \right|, \quad (7)$$

$$C_3 = \sum_{n=3}^{N_{ap}} \left| \frac{S_{2(n),1(1)}^{EHMV}}{S_{2(1),1(1)}^{EHMV}} \right| + \sum_{n=3}^{N_{ap}} \left| \frac{S_{2(n),1(1)}^{EHMV}}{S_{2(1),1(1)}^{EHMV}} \right| + \sum_{n=3}^{N_{ap}} \left| \frac{S_{2(n),1(1)}^{MHMV}}{S_{2(1),1(1)}^{MHMV}} \right|, \quad (8)$$

$$C_4 = \max_f \left\{ \left| S_{1(1),1(1)}^{EHMV}(f) \right| \right\} + \max_f \left\{ \left| S_{1(1),1(1)}^{EHMV}(f) \right| \right\} + \max_f \left\{ \left| S_{1(1),1(1)}^{MHMV}(f) \right| \right\}, \quad (9)$$

where C_1 and C_2 represent, respectively, the magnitude and phase error of the three modal function pairs, C_3 expresses the transmission to higher order modes, and C_4 takes into account the return loss at the mode converter rectangular waveguide ports.

It should be stressed that the terms (6)–(8) are computed at the central frequency of the operation band ($f_0 = 35$ GHz) while the three terms of (9) are computed as the maximum over the operation band.

After this initial optimization the mode converter and the horn are reoptimized together, adjusting not only the design parameters of the mode converter but also the reference radii of the horn. The same cost function (5) is used but in this case the optimization parameters are not only the dimensions of the waveguide sections that form the mode converter but also the reference radii of the horn. Therefore at each iteration of the optimization process it is necessary to perform an analysis not only of the mode converter but of the ensemble formed by both devices.

Table IV shows the obtained (after the whole optimization process) modal amplitudes at the horn aperture of the first ten modes (at the central frequency) for the three sets of excitations at the rectangular ports of the mode converter. As it can be appreciated, in the three cases the complex amplitude of the first two modes present the appropriate values (both in magnitude and phase) to generate their corresponding radiation pattern as indicated by Table II. In addition, amplitudes of the higher order modes are very small compared with the main modes involved in each pattern.

IV. SIMULATION OF THE COMPLETE MONOPULSE FEED

This section shows the simulated results for the final designed feed using three different numerical tools: mode-matching in-house code, CST Microwave Studio [47] and Ansys HFSS [48]. The mode-matching approach has already been used in the optimization process for the mode converter and the horn, assuming that the excitations produced by the comparator network at the rectangular ports of the mode converter are perfect (i.e. they all have the same magnitude and the phase differences are those of Fig. 3). This assumption is reasonable given the results of the comparator network in Figs. 11–15.

The CST and HFSS results correspond to the whole feed structure. In order to achieve a more efficient simulation the device is divided in two parts: the comparator network is simulated as a closed problem

TABLE IV
COMPLEX MODAL AMPLITUDES AT THE HORN APERTURE CORRESPONDING TO EACH OF THE THREE RADIATION PATTERNS. FOR EACH CASE THE VALUES ARE NORMALIZED TO THAT OF THE FUNDAMENTAL MODE. THE PHASE VALUES ARE IN RADIAN.

Sum (EHMV)				Azim. Diff. (EHEV)				Elev. Diff. (MHMV)			
Mode	Magnitude	Phase	f_c (GHz)	Mode	Magnitude	Phase	f_c (GHz)	Mode	Magnitude	Phase	f_c (GHz)
TE_{c11}	1.00	0.00	3.2	TE_{c21}	1.00	0.00	5.3	TM_{c01}	1.00	0.00	4.2
TM_{s11}	0.41	3.14	6.7	TE_{c01}	1.00	3.14	6.7	TE_{s21}	1.00	0.00	5.3
TE_{c31}	0.05	2.06	7.3	TM_{s21}	0.12	4.75	9.0	TM_{c21}	0.12	1.61	9.0
TE_{c12}	0.14	1.65	9.3	TE_{c41}	0.00	7.38	9.3	TE_{s41}	0.00	-0.70	9.3
TM_{s31}	0.01	0.57	11.1	TE_{c22}	0.02	7.02	11.7	TM_{c02}	0.23	1.73	9.6
TE_{c51}	0.00	0.00	11.2	TE_{c02}	0.02	4.85	12.3	TE_{s22}	0.02	0.74	11.7
TM_{s12}	0.07	0.60	12.3	TE_{c61}	0.00	6.28	13.1	TE_{s61}	0.00	0.00	13.1
TE_{c32}	0.01	3.34	14.0	TM_{s41}	0.00	6.58	13.3	TM_{c41}	0.00	1.64	13.3
TE_{c13}	0.02	2.84	14.9	TM_{s22}	0.01	7.51	14.7	TM_{c22}	0.01	4.37	14.7
TE_{c71}	0.00	0.00	15.0	TE_{c42}	0.00	9.06	16.2	TM_{c03}	0.05	2.80	15.1

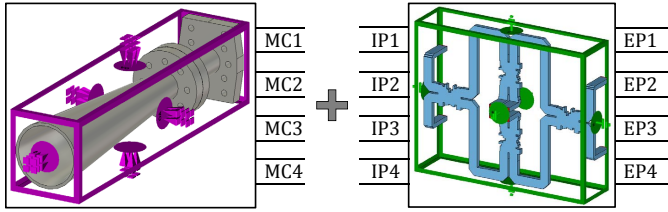


Fig. 19. Schematic representation of the approach followed for the full-wave simulations of the complete antenna feed.

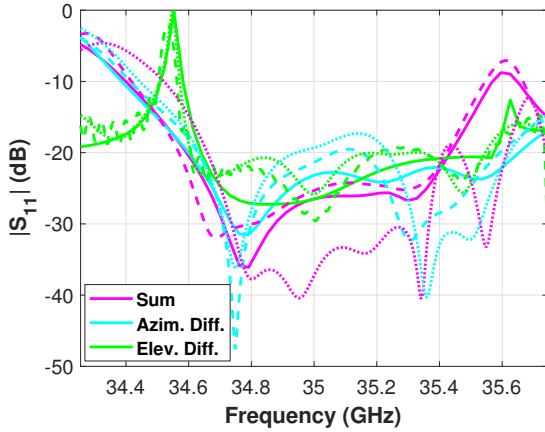


Fig. 20. Full-wave simulation of the reflection coefficient results corresponding to the complete monopulse feed obtained by the mode-matching approach (solid), and also by CST (dashed) and HFSS (dotted) simulating separately the comparator network and the horn with the mode converter.

and the mode converter and horn are simulated together with open (radiation) boundary conditions. Then the results of both simulations are combined to obtain the simulated results for the whole monopulse feed. This simulation strategy is illustrated in Fig. 19.

These results are represented in Figs. 20, 21. In general there is very good agreement between the three simulations. First of all, it can be appreciated that the reflection coefficient values are below -20 dB in the design band (except the azimuthal difference case in the HFSS simulation). Additionally, the radiation pattern specifications of Table I are fulfilled.

V. PROTOTYPE MANUFACTURING

In order to demonstrate the feasibility of the proposed design, a prototype has been manufactured and characterized experimentally.

The different components of the antenna have been built using diverse techniques. The horn has been machined using a lathe. During this process, it was specially important to control any vibrations of the part rotating in the lathe since, due to the relatively great length, any small perturbation may have a significant impact on the symmetry of the resulting device.

Given its intricate inner geometry, the mode converter has been built using Electrical Discharge Machining (EDM) since it was not possible to build all the inner cavities using conventional milling. Indeed it has been necessary to manufacture the component in two different parts so that the EDM tool could access properly all the waveguide sections.

Finally, the comparator network has been built in two parts following the typical division in body and cover. The body has been machined using conventional H-plane milling. EDM was used for the waveguide sections corresponding to the external ports, since these waveguides were too deep for the drill. Additionally, four rectangular apertures have been opened at the cover in order to create the internal ports that connect with the mode converter. It must be taken into account that the H-plane milling produces a certain rounding of the concave corners and therefore the effect of this rounding must be studied prior to the manufacturing. To address this, the comparator network including the 180° hybrid couplers has been simulated considering a rounding of the corners with a 0.75 mm radius (which corresponds to a drill big enough to be used comfortably during the milling process) and no noticeable difference has been found in the scattering parameters. Moreover, the impact of the tolerances in the corrugations of the coupler has to be studied in detail to prevent the deterioration of the phase response. The manufacturer guaranteed a ± 0.03 mm tolerance for the H-plane milling parts. This tolerance has been studied by means of simulations but it did not produce any significant effect in the performance of the coupler.

All the parts have been manufactured using aluminium 6082-T6 [49, Ch. 6] and after machining them they have been treated with a chromate conversion coating [50]. Additionally it is important to emphasize that, as it is usual in waveguide designs at these frequencies, special care had to be taken in the assembly of the different parts, using pins to guarantee the proper alignment of all the pieces and fastening them with enough screws to guarantee a good electrical contact. In the next section it will be studied how the contact between device parts can affect the power losses.

VI. EXPERIMENTAL RESULTS

First the scattering parameters of the feed have been measured using a vector network analyser. The obtained results are presented in Fig. 22. It can be appreciated that the reflection coefficient level

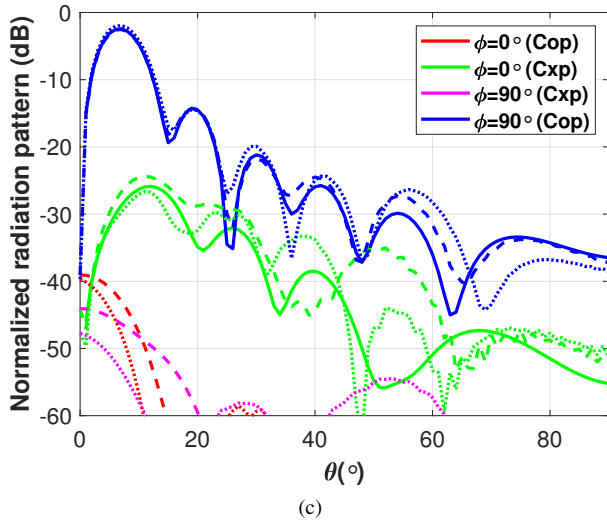
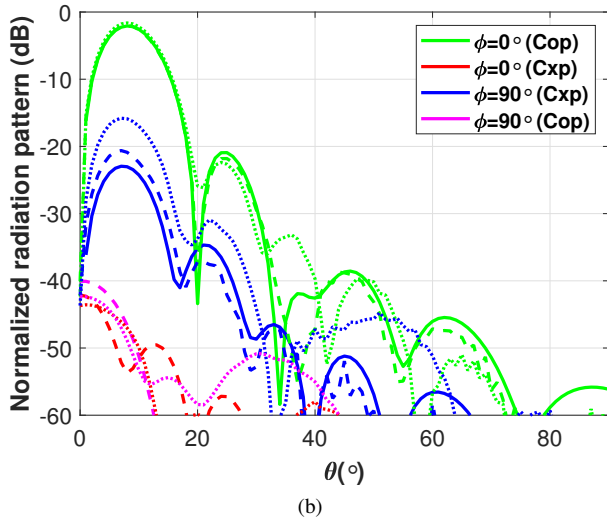
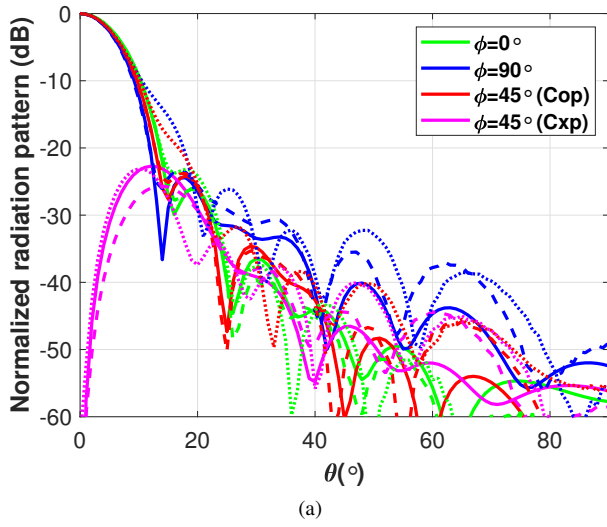


Fig. 21. Simulated radiation pattern results obtained using mode-matching (solid), CST (dashed) and HFSS (dotted): (a) Sum pattern $D_{0,MM} = 24.76$ dBi, $D_{0,CST} = 24.80$ dBi, $D_{0,HFSS} = 24.30$ dBi. (b) Azimuthal difference pattern $D_{0,MM} = 22.69$ dBi, $D_{0,CST} = 22.80$ dBi, $D_{0,HFSS} = 22.67$ dBi. (c) Elevation difference pattern $D_{0,MM} = 22.31$ dBi, $D_{0,CST} = 22.27$ dBi, $D_{0,HFSS} = 22.37$ dBi.

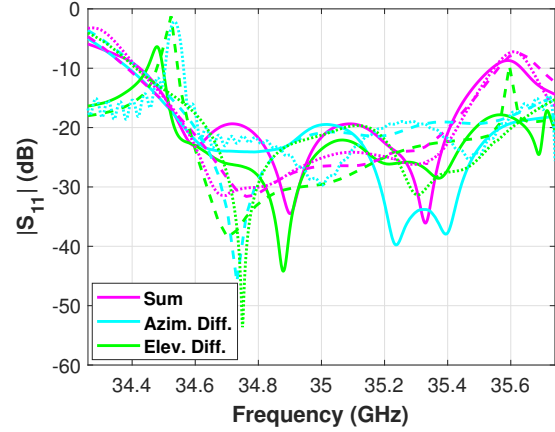


Fig. 22. Measured reflection at the ports corresponding to the three radiation patterns (solid line) compared with the values simulated by mode-matching (dashed line) and CST (dotted line).



Fig. 23. Photograph of the prototype during the measurement of the radiation characteristics.

measured at the external ports is below -20 dB for the design band (34.6 GHz to 35.4 GHz).

After this, the radiation characteristics of the feed (radiation pattern, directivity and gain) have been measured at an anechoic chamber (see Fig. 23). The obtained radiation pattern, compared with the mode-matching and CST simulations, is depicted in Fig. 24. As it can be appreciated there is good agreement between the simulated and measured values. The only noticeable differences are in the cross-polarization level of the sum and azimuthal difference patterns. In the first case the measured cross-polarized radiation level is -20.6 dB, which is slightly greater than the simulated one. However small deviances like this can be explained by the asymmetries in the device due to manufacturing tolerances and therefore they already were expected. On the other hand, the cross-polarization level measured for the azimuthal difference pattern is some decibels better than the value predicted by the simulation.

The measured directivity and gain values are presented in Table V. It can be appreciated that the measured power losses of the device are between 0.65 dB and 0.80 dB depending on the chosen radiation pattern. The table also shows the simulated directivity and gain values. Two groups of simulated values are presented. The first one (referred to as “ideal”) corresponds to a simulation where the

TABLE V
COMPARISON OF THE MEASURED AND SIMULATED DIRECTIVITY (D_0) AND GAIN (G_0) VALUES (dBi) WITH CORRESPONDING LOSSES (dB).

		Simulation (ideal)			Simulation (realistic)			Measurements		
		D_0	G_0	Losses	D_0	G_0	Losses	D_0	G_0	Losses
Sum	34.6 GHz	23.92	23.80	0.12	23.92	23.13	0.79	23.84	23.07	0.77
	35.0 GHz	24.84	24.75	0.09	24.84	24.06	0.78	24.85	24.08	0.77
	35.4 GHz	25.07	25.04	0.03	25.07	24.33	0.74	25.10	24.31	0.79
Azim. Diff.	34.6 GHz	21.30	21.14	0.16	21.30	20.46	0.84	21.37	20.72	0.65
	35.0 GHz	22.76	22.60	0.16	22.76	21.89	0.87	22.66	21.98	0.68
	35.4 GHz	19.69	19.59	0.10	19.69	18.90	0.79	18.66	18.01	0.65
Elev. Diff.	34.6 GHz	22.16	22.04	0.12	22.16	21.45	0.71	22.32	21.63	0.69
	35.0 GHz	22.33	22.24	0.09	22.33	21.54	0.79	22.44	21.79	0.65
	35.4 GHz	22.35	22.25	0.10	22.35	21.51	0.84	22.44	21.75	0.69

conductivity of the antenna metallic parts is set to that of the aluminium ($\sigma_{Al} = 3.6 \times 10^7$ S/m). As it can be appreciated the power losses estimated by this simulation are significantly lower than the measured ones.

One of the causes of this difference is the roughness of the waveguide walls produced by the machining, which causes the effective conductivity of the device to be lower than that of the material used in the manufacturing. An additional cause of power losses is the electrical contact between the body and cover of the comparator network. Although both parts are strongly tightened by carefully placed screws, even a very small separation between them can produce an increment of the power losses. To incorporate these effects into the simulation the electrical conductivity of the waveguide walls is set to $0.5 \cdot \sigma_{Al}$ and the comparator network body and cover are separated $4 \mu\text{m}$. The results of this new simulation are presented at Table V labelled as “realistic” and it can be appreciated that in this case the simulated power losses are closer to the measured values, specially for the sum pattern. The small differences observed for the difference pattern can be explained by the difficulties of accurately measuring the gain of an antenna with an off-boresight main lobe. Taking into account the inherent uncertainty associated to any experimental setup, the observed difference between the measured and simulated values can be considered acceptable.

The results obtained by the proposed device are compared with other state-of-the-art works in Table VI. First of all it can be observed that only [25] presents a design where a single horn feed is used. In the rest of the works the monopulse patterns are generated by using arrays. Additionally, while the proposed device is optimized to achieve a return loss level of 20 dB, the other designs are optimized for a 10 dB level. Moreover, in most of the other works obtaining a low cross polarization level at the $\phi = 45^\circ$ plane is not enforced. Only [34] presents a cross polarization result at the diagonal plane, which is indeed 2.4 dB better than the result obtained by the present work. However it should be emphasized that the design in [34] presents a single difference pattern and additionally the antenna is implemented at a much lower frequency, which significantly reduces the effect of the manufacturing tolerance.

VII. CONCLUSION

This work has presented the design and prototyping of a triple radiation pattern monopulse feed based on a spline profile high-gain horn, connected through a mode converter to a comparator network. The comparator network has been implemented in a single level, which leads to a very compact topology and also reduces its manufacturing complexity to a quasi 2D approach based on a body and a lid.

This single level implementation has been possible thanks to the introduction of a novel H-plane 180° waveguide coupler. These couplers avoid the use of other more cumbersome structures as magic-Ts and the need of introducing additional phase shifters in the network. Finally, the mode converter generates the circular waveguide modes that produce the different radiation patterns. It is worth noting that each of the three radiation patterns is generated by the combination of two modal field functions with a certain relative amplitude and phase. The experimental results for the three patterns are in very good agreement with the simulations, showing the potential of the presented antenna feed for monopulse applications.

REFERENCES

- [1] J. B. McKinney, “Radar: a reluctant miracle,” *IEEE Aerospace and Electronic Systems Magazine*, vol. 21, no. 8, pp. ix–xviii, Aug 2006.
- [2] G. J. Frazer and C. G. Williams, “Decametric radar for missile defence,” in *2019 IEEE Radar Conference (RadarConf)*, April 2019, pp. 1–6.
- [3] M. E. Davis, “A history of battlefield surveillance radar,” in *2015 IEEE Radar Conference (RadarCon)*, May 2015, pp. 1345–1350.
- [4] T. F. Brukiewa, “Active array radar systems applied to air traffic control,” in *Proceedings of IEEE National Telesystems Conference - NTC '94*, May 1994, pp. 27–32.
- [5] T. Shejbal, P. Bezousek, and T. Zalabsky, “Active antenna array concepts for precision approach radar,” in *Proceedings ELMAR-2014*, Sep. 2014, pp. 1–4.
- [6] G. Clementi, C. Migliaccio, N. Fortino, J. Dauvignac, J. Willebois, and C. Chekroun, “Wideband antenna for land-mine detection radar,” in *2014 International Radar Conference*, Oct. 2014, pp. 1–4.
- [7] Z. Wang, S. Gogineni, F. Rodriguez-Morales, J. Yan, J. Paden, C. Leuschen, R. D. Hale, J. Li, C. L. Carabajal, D. Gomez-Garcia, B. Townley, R. Willer, L. Stearns, S. Child, and D. Braaten, “Multi-channel wideband synthetic aperture radar for ice sheet remote sensing: Development and the first deployment in Antarctica,” *IEEE Journal of Selected Topics in Applied Earth Observations and Remote Sensing*, vol. 9, no. 3, pp. 980–993, March 2016.
- [8] A. Kuriyama, H. Nagaishi, H. Kuroda, and K. Takano, “A high efficiency antenna with horn and lens for 77 GHz automotive long range radar,” in *2016 European Radar Conference (EuRAD)*, Oct. 2016, pp. 378–381.
- [9] Yeonghwan Ju, Youngseok Jin, and Jonghun Lee, “Design and implementation of a 24 GHz FMCW radar system for automotive applications,” in *2014 International Radar Conference*, Oct 2014, pp. 1–4.
- [10] S. Knyazev and S. Shabunin, “Antenna systems for the meteorological radar design,” in *2006 European Radar Conference*, Sep. 2006, pp. 206–208.
- [11] S. Tanelli, Z. S. Haddad, E. Im, S. L. Durden, O. O. Sy, E. Peral, G. A. Sadowy, and M. Sanchez-Barberty, “Radar concepts for the next generation of spaceborne observations of cloud and precipitation processes,” in *2018 IEEE Radar Conference (RadarConf18)*, April 2018, pp. 1245–1249.
- [12] E. Garcia-Marin, J. L. Masa-Campos, and P. Sanchez-Olivares, “W-band array antenna for radar detection of space debris,” in *12th European Conference on Antennas and Propagation (EuCAP 2018)*, April 2018, pp. 1–4.

TABLE VI
COMPARISON OF SOME CHARACTERISTICS OF THE ARRAY IMPLEMENTED IN THIS WORK WITH OTHER WORKS IN THE STATE OF THE ART.

Parameter	This work	[25]	[51]	[33]	[34]	[52]
f_0 (GHz)	35	93	15	2.8	7	93
Double/Triple Pattern	Triple	Triple	Triple	Double	Double	Triple
Δ_{BW} (%) @20dB	2.3	3.0	1.7	–	2.0	–
Δ_{BW} (%) @10dB	3.0	4.3	13.4	28.6	126	6.7
Isolation (dB)	33.3	25	30	25	15	30
Sum Gain (dBi)	24.08	20	32	14	13.1	35.6
Diff. Gain (dBi)	21.8	18	N/A	11.6	10.6	31.6
Sum Crosspolarization (dB) @ $\phi = 45^\circ$	-20.6	N/A	N/A	N/A	-23	N/A
Diff. Crosspolarization (dB)	-21.4	N/A	N/A	N/A	N/A	N/A
Sum SLL (dB) w.r.t. Sum max	-24.8	-11	-13	-10	-17.5	-21
Azim. Diff. SLL (dB) w.r.t. Sum max	-21.7	N/A	-10	N/A	N/A	-19.1
Elev. Diff. SLL (dB) w.r.t. Sum max	-14.2	N/A	-10.0	-20.0	-10.0	-13.1
Technology	Waveguide Circular horn	Waveguide Pyramidal horn	Waveguide 16x16 array of slots	Planar 4x1 Yagi array	Planar 2x1 Vivaldi array	Waveguide Array of 752 box horns

- [13] A. Tamayo-Domínguez, J. Fernández-González, and M. Sierra-Castañer, "Monopulse RLSA antenna with gap-waveguide feeding network for space debris radar at 94 GHz," in *2018 48th European Microwave Conference (EuMC)*, Sep. 2018, pp. 400–403.
- [14] W. D. Fitzgerald, "A 35-GHz beam waveguide system for the millimeter-wave radar," *Lincoln Laboratory Journal*, vol. 5, no. 2, pp. 245–272, Jan. 1992.
- [15] H. Huang, B. Wang, F. Li, and Lu Zhao, "A Ka-band monopulse microstrip antenna array," in *2008 IEEE MTT-S International Microwave Workshop Series on Art of Miniaturizing RF and Microwave Passive Components*, Dec. 2008, pp. 124–127.
- [16] A. Brokmeier, T. Geist, B. Zimmermann, and R. Mack, "A miniaturised frontend for Ka-band radar applications," in *2005 European Microwave Conference*, vol. 3, Oct. 2005, pp. 4 pp.2091–2094.
- [17] M. Skolnik, *Introduction to Radar Systems*, 2nd ed., ser. Electrical engineering series. McGraw-Hill, 1980.
- [18] S. Sherman and D. Barton, *Monopulse Principles and Techniques*, ser. Artech House radar library. Artech House, 2011.
- [19] D. K. Barton, "Development of the AN/FPS-16 instrumentation radar," *IEEE Aerospace and Electronic Systems Magazine*, vol. 26, no. 4, pp. B1–B16, April 2011.
- [20] J. Kuecken, "Feed optimization in multi-feed antennas," in *WESCON/57 Conference Record*, vol. 1, Aug 1957, pp. 164–179.
- [21] P. Hannan, "Optimum feeds for all three modes of a monopulse antenna ii: Practice," *IRE Transactions on Antennas and Propagation*, vol. 9, no. 5, pp. 454–461, Sep. 1961.
- [22] J. Shelton, "Improved feed design for amplitude monopulse radar antennas," in *1958 IRE International Convention Record*, vol. 7, March 1959, pp. 93–102.
- [23] A. Olver, P. Clarricoats, A. Kishk, and L. Shafai, *Microwave Horns and Feeds*, ser. Electromagnetic waves series. London, UK and New York, USA: IEE, 1994.
- [24] P. J. B. Clarricoats and R. D. Elliot, "Multimode corrugated waveguide feed for monopulse radar," *IEE Proceedings H - Microwaves, Optics and Antennas*, vol. 128, no. 2, pp. 102–110, April 1981.
- [25] R. Shen, X. Ye, and J. Miao, "Design of a multimode feed horn applied in a tracking antenna," *IEEE Transactions on Antennas and Propagation*, vol. 65, no. 6, pp. 2779–2788, June 2017.
- [26] R. J. Liu and W. B. Dou, "Design and analysis of 3mm multimode monopulse feed," in *2007 International Conference on Microwave and Millimeter Wave Technology*, April 2007, pp. 1–4.
- [27] W. Hongjian, "Multimode horn for a monopulse subsystem," in *2019 IEEE International Symposium on Antennas and Propagation and UNSC-URSI Radio Science Meeting*, July 2019, pp. 1645–1646.
- [28] A. K. Pandey, "Design of multimode tracking system for earth station antenna," in *2016 Asia-Pacific Microwave Conference (APMC)*, Dec. 2016, pp. 1–4.
- [29] B. K. Watson, N. D. Dang, and S. Ghosh, "A mode extraction network for rf sensing in satellite reflector antenna," in *2nd International Conference on Antennas and Propagation*, Jan 1981, pp. 323–327.
- [30] A. M. El-Tager, H. N. Ahmad, and M. M. Darwish, "Multimode antenna feed system for an X-band monopulse radar," in *2009 IEEE Radar Conference*, May 2009, pp. 1–4.
- [31] T. Yang, Z. Zhao, D. Yang, X. Liu, and Q. Liu, "A single-layer SIW slots array monopulse antenna excited by a dual-mode resonator," *IEEE Access*, vol. 7, pp. 131 282–131 288, 2019.
- [32] F. Cao, D. Yang, J. Pan, D. Geng, and H. Xiao, "A compact single-layer substrate-integrated waveguide (SIW) monopulse slot antenna array," *IEEE Antennas and Wireless Propagation Letters*, vol. 16, pp. 2755–2758, 2017.
- [33] X. Nie, W. Hong, and K. Fan, "Monopulse array and low side-lobe level array with a novel feed network," *IET Microwaves, Antennas Propagation*, vol. 12, no. 12, pp. 1978–1985, 2018.
- [34] Y. Wang, G. Wang, Z. Yu, J. Liang, and X. Gao, "Ultra-wideband E-plane monopulse antenna using vivaldi antenna," *IEEE Transactions on Antennas and Propagation*, vol. 62, no. 10, pp. 4961–4969, 2014.
- [35] H. Chen, W. Che, Q. He, W. Feng, X. Wei, and K. Wu, "Compact substrate integrated waveguide (SIW) monopulse network for Ku-band tracking system applications," *IEEE Transactions on Microwave Theory and Techniques*, vol. 62, no. 3, pp. 472–480, March 2014.
- [36] X. Xu, J. Hirokawa, and M. Ando, "Double-layered plate-laminated waveguide monopulse comparator in E-band," in *2016 IEEE International Symposium on Antennas and Propagation (APS-URSI)*, June 2016, pp. 1703–1704.
- [37] H. Kumar, G. Kumar, Y. Verma, and P. K. Mishra, "Compact waveguide monopulse comparator at Ka-band for monopulse tracking," in *2016 IEEE International Symposium on Antennas and Propagation (APS-URSI)*, June 2016, pp. 1357–1358.
- [38] T. Das and V. K. Singh, "Broadband waveguide monopulse comparator at X-band," in *2017 International Conference on Innovations in Electronics, Signal Processing and Communication (IESC)*, April 2017, pp. 181–185.
- [39] C. Granet, G. L. James, R. Bolton, and G. Moorey, "A smooth-walled spline-profile horn as an alternative to the corrugated horn for wide band millimeter-wave applications," *IEEE Transactions on Antennas and Propagation*, vol. 52, no. 3, pp. 848–854, March 2004.
- [40] D. Pozar, *Microwave Engineering*. Wiley, 2004.

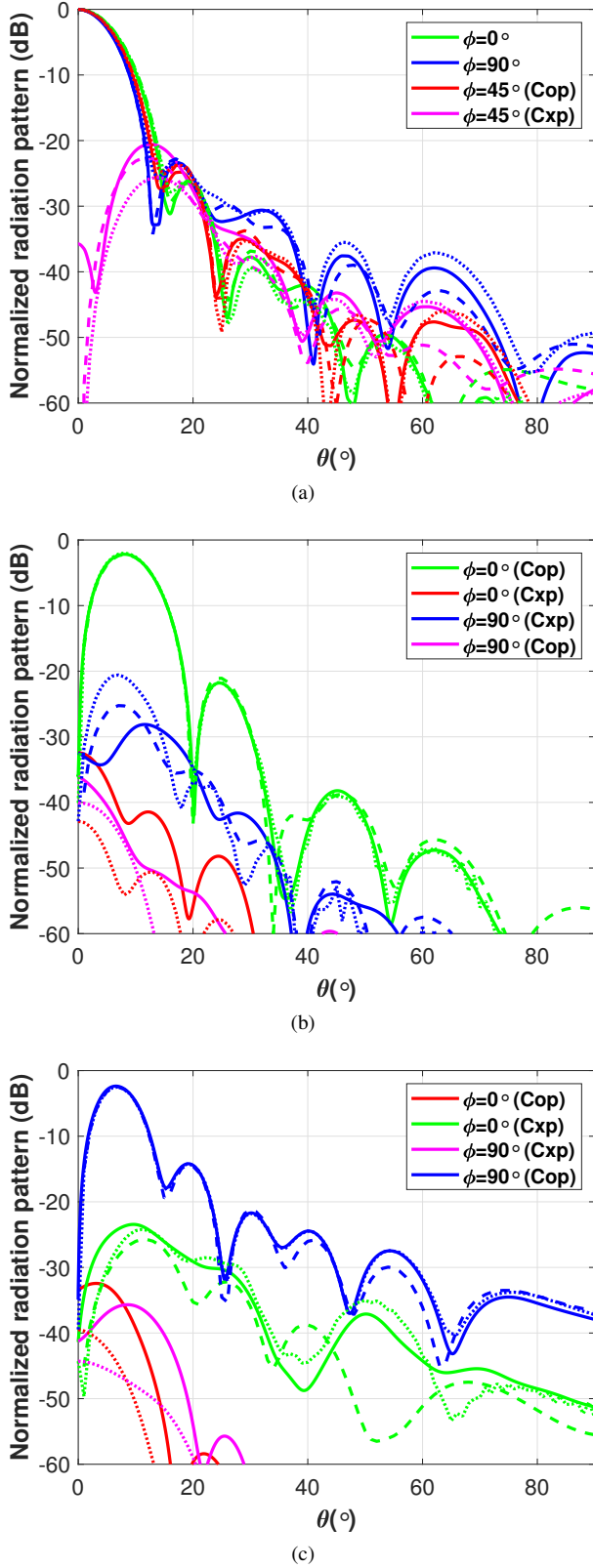


Fig. 24. Measured radiation pattern (solid line) of the complete monopulse feed compared with the mode-matching (dashed line) and CST (dotted line) simulations: (a) Sum pattern $D_{0,Meas} = 24.85$ dBi, $D_{0,MM} = 24.76$ dBi, $D_{0,CST} = 24.84$ dBi. (b) Azimuthal difference pattern $D_{0,Meas} = 22.66$ dBi, $D_{0,MM} = 22.14$ dBi, $D_{0,CST} = 22.76$ dBi. (c) Elevation difference pattern $D_{0,Meas} = 22.44$ dBi, $D_{0,MM} = 22.16$ dBi, $D_{0,CST} = 22.33$ dBi.

- [41] B. Liu, W. Hong, Z. Kuai, X. Yin, G. Luo, J. Chen, H. Tang, and K. Wu, "Substrate integrated waveguide (SIW) monopulse slot antenna array," *IEEE Transactions on Antennas and Propagation*, vol. 57, no. 1, pp. 275–279, 2009.
- [42] H. Riblet, "The short-slot hybrid junction," *Proceedings of the IRE*, vol. 40, no. 2, pp. 180–184, Feb 1952.
- [43] G. Conciauro, M. Guglielmi, and R. Sorrentino, *Advanced modal analysis: CAD techniques for waveguide components and filters*. Wiley, 2000.
- [44] J. A. Ruiz-Cruz, J. R. Montejo-Garai, and J. M. Rebollar, *Passive Microwave Components and Antennas*. In-Tech, 2010, ch. "Computer Aided Design of Waveguide Devices by Mode-Matching Methods".
- [45] L. Polo-López, J. A. Ruiz-Cruz, J. R. Montejo-Garai, and J. M. Rebollar, "Analysis of waveguide devices involving lateral and transverse perfect magnetic wall boundary conditions by the mode-matching method," *Radio Science*, vol. 52, no. 9, pp. 1223–1234, 2017.
- [46] W. L. Stutzman and G. Thiele, *Antenna theory and design*. Wiley, 1998.
- [47] "CST Microwave Studio 2018," <https://www.cst.com/>, accessed: 2019-08-12.
- [48] "ANSYS High Frequency Structure Simulator 19.0.0," <https://www.ansys.com/>, accessed: 2019-08-12.
- [49] E. Avallone, T. Baumeister, and A. Sadegh, *Marks' Standard Handbook for Mechanical Engineers*, 10th ed., ser. McGraw-Hill's AccessEngineering. McGraw-Hill, 1996.
- [50] *Bonderite M-CR 1200 Aero*, Henkel AG & Co. KGaA, Feb. 2015.
- [51] G. Huang, S. Zhou, and T. Chio, "Highly-efficient self-compact monopulse antenna system with integrated comparator network for RF industrial applications," *IEEE Transactions on Industrial Electronics*, vol. 64, no. 1, pp. 674–681, Jan 2017.
- [52] R. Shen, X. Ye, J. Xie, Z. Chen, and C. Jin, "A W-band circular box-horn antenna array radiating sum and difference beams with suppressed sidelobe," *IEEE Transactions on Antennas and Propagation*, vol. 67, no. 9, pp. 5934–5942, 2019.